POLYOXOMETALATES

Open Access
RESEARCH ARTICLE

Rational design of hexanuclear zirconium-cluster-based porphyrinic metal-organic frameworks for high-efficiency electrocatalytic nitrate reduction to ammonia

Liqing Li, Xinming Wang ✉, Jian Li, Yufang Wang, Haijun Pang ✉, and Huiyuan Ma

School of Materials Science and Chemical Engineering, Harbin University of Science and Technology, Harbin 150040, China

Cite This: *Polyoxometalates*, **2026**, *5*, 9140116

Read Online

ABSTRACT: Green ammonia (NH_3) synthesis is pivotal for sustainable agriculture and hydrogen energy carriers; however, challenges persist in direct electrocatalytic nitrate reduction (e-NO_3RR) under neutral conditions, including competing hydrogen evolution and sluggish reaction kinetics. Herein, a series of transition-metal–porphyrin metal-organic frameworks (MOFs), NU-902(M) (M = Fe, Co, Ni, Cu), are engineered via coordination between metalated tetrakis(4-carboxyphenyl)porphyrin (M-TCPP) and $Zr_6O_4(OH)_4(CO_2)_{12}$ clusters, constructing a hierarchical mesoporous architecture. Notably, NU-902(Cu) achieves a Faradaic efficiency (FE) of 71.65% with an NH_3 yield rate of 13.76 $mg \cdot h^{-1} \cdot mg_{cat.}^{-1}$ at −0.9 V vs. reversible hydrogen electrode (RHE), outperforming analogous frameworks based on Fe (14.01 $mg \cdot h^{-1} \cdot mg_{cat.}^{-1}$, 63.83%), Co (9.51 $mg \cdot h^{-1} \cdot mg_{cat.}^{-1}$, 71.51%), and Ni (2.40 $mg \cdot h^{-1} \cdot mg_{cat.}^{-1}$, 67.99%). Moreover, the FE of NU-902(Cu) remains above 65% after 500 cycles, and powder X-ray diffraction characterization confirms no significant collapse of the framework structure, indicating excellent structural stability. This work establishes porphyrinic MOFs as efficient platforms for sustainable nitrogen valorization and provides experimental guidance for modulating metal-specific activity in electrocatalysis.

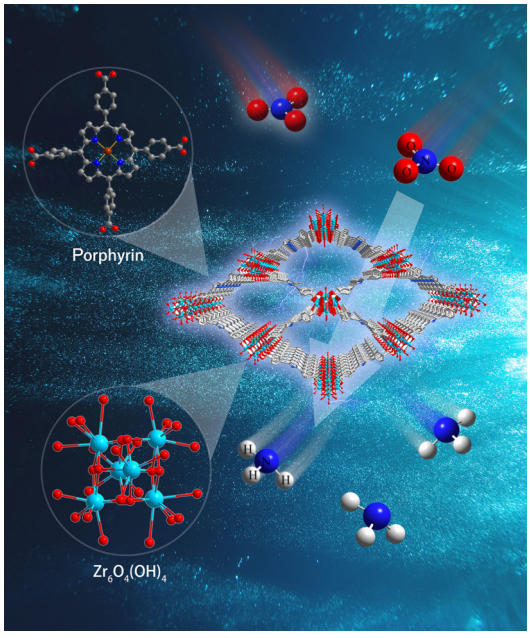

KEYWORDS: porphyrinic metal-organic frameworks, green ammonia synthesis, copper electrocatalyst, electrocatalytic nitrate reduction

1 Introduction

Ammonia (NH_3) is not only the core raw material for nitrogen fertilizers, with approximately 80% of global ammonia production used for fertilizer manufacture, but also a potential key carrier in future clean energy systems, such as liquid ammonia for hydrogen storage and fuel cell applications. However, since its invention in the early 20th century, the traditional Haber–Bosch process has increasingly revealed its reliance on fossil fuels and the associated high carbon emissions [1–4]. This process requires extreme operating conditions (400–500 °C, 15–25 MPa), consumes approximately 1%–2% of the global energy supply annually, and emits more than 450 million tons of CO_2, accounting for about 1.3% of global emissions [5–8]. With the advancement of the "dual carbon" goals, the development of green and low-carbon ammonia synthesis technologies has become increasingly urgent [9–11].

In recent years, electrocatalytic ammonia synthesis has attracted significant attention due to its ability to utilize renewable energy sources, such as wind and solar power, under ambient temperature and pressure [12, 13]. This technology primarily involves two pathways: nitrogen reduction (NRR) and nitrate reduction (NO_3RR). NRR directly employs nitrogen as the reactant; however, it is limited by the high activation energy of nitrogen, as the bond energy of N≡N is 941 $kJ \cdot mol^{-1}$, and by competition with the hydrogen evolution reaction (HER) [14, 15]. At present, the highest reported Faradaic efficiency (FE) is approximately 60%, while the ammonia yield is generally below 0.1 $mg \cdot h^{-1} \cdot cm^{-2}$ [16, 17]. In contrast, electrocatalytic nitrate reduction uses nitrate (NO_3^-) derived from industrial wastewater and agricultural runoff as the nitrogen source, offering simultaneous pollution control and

Received: September 30, 2025; **Revised:** December 19, 2025
Accepted: January 11, 2026

✉Address correspondence to Xinming Wang, wangxinming20@126.com; Haijun Pang, panghj116@163.com

https://doi.org/10.26599/POM.2026.9140116

resource recovery. Therefore, this strategy is considered one of the most promising approaches for potentially replacing the Haber–Bosch process to achieve green and sustainable NH_3 synthesis [18, 19].

The efficiency and selectivity of the nitrate reduction process are highly dependent on catalyst design. Existing catalysts can be broadly classified into noble-metal-based catalysts, nonnoble transition-metal catalysts, alloy catalysts, and single-atom catalysts [20]. Although these catalyst systems have achieved varying degrees of progress, many conventional catalysts struggle to maintain high performance under neutral conditions. This limitation highlights the need for innovative catalyst designs that integrate high dispersion of active sites with structural robustness [21]. In this context, metal-organic frameworks (MOFs) have attracted considerable attention as promising electrocatalysts for nitrate reduction, owing to their highly tunable structures and multifunctional active sites [22, 23]. Constructed from metal nodes and organic ligands linked by coordination bonds, MOFs possess crystalline porous frameworks with ultrahigh surface areas and well-defined pore channels [24–31], which facilitate mass transport and improve the accessibility of nitrate ions to active sites [32–36]. Among various MOF families, porphyrin-based MOFs have emerged as a particularly attractive subclass for electrocatalysis [37, 38]. These materials combine structural regularity, high surface area, and design flexibility with well-isolated metal–N4 sites that resemble those found in biological catalysts. Notably, zirconium-based porphyrinic MOFs, such as UiO-66, PCN-222, and NU-902, exhibit exceptional chemical stability owing to the high bond dissociation energy of Zr–O bonds, approximately 776 $kJ·mol^{-1}$ [39]. This robustness enables postsynthetic metallation of porphyrin centers with transition metals, including Fe, Co, Ni, and Cu, allowing precise construction of catalytically active $M–N_4$ sites within the framework [21]. The introduced metal centers not only regulate electronic structures and promote electron transfer through d–π conjugation but also strengthen the adsorption of key reaction intermediates [40, 41], thereby lowering activation barriers in processes such as nitrate reduction to ammonia. For example, molecular-level hydrophobic modification of Fe-PCN-222 through alkyl chain grafting was reported to suppress competing reactions and achieve a FE of 70.7% for nitrate electroreduction [42]. Collectively, these zirconium-based porphyrin MOFs, which integrate structural stability with tunable catalytic properties, provide valuable insights for the development of efficient and durable catalysts for electrochemical ammonia synthesis from nitrate [43].

This paper focuses on zirconium-based porphyrinic MOFs through the design and synthesis of transition-metal-substituted porphyrin ligands (M-TCPP, M = Fe, Co, Ni, Cu). The NU-902(M) series was prepared via one-step solvothermal synthesis. Powder X-ray diffraction (PXRD), Fourier transform infrared (FT-IR) spectroscopy, X-ray photoelectron spectroscopy (XPS), scanning electron microscopy (SEM), and transmission electron microscopy (TEM) were employed to characterize the composition and morphology of the materials. In addition, cyclic voltammetry, linear sweep voltammetry (LSV), electrochemical impedance spectroscopy (EIS), and chronoamperometric measurements were used to evaluate their electrocatalytic nitrate reduction performance under neutral conditions (0.1 M $NaNO_3$ and 0.1 M Na_2SO_4), which represent the most widely studied and practically promising reaction environment. The introduced transition metals form stable $metal–N_4$ catalytic active centers, significantly enhancing reaction kinetics and imparting excellent nitrate reduction activity and electrochemical stability. Among the investigated catalysts, NU-902(Cu) exhibited the best performance, achieving a FE of 71.65% and an ammonia yield rate of 13.76 $mg·h^{-1}·mg_{cat.}^{-1}$ at −0.9 V vs. reversible hydrogen electrode (RHE), outperforming the corresponding Fe-, Co-, and Ni-based frameworks.

2 Experimental section

The preparation process of NU-902(M) is illustrated in Fig. 1(a). First, 11 mg of zirconium oxychloride octahydrate and 750 mg of benzoic acid were placed in a glass vial, followed by the addition of 10 mL of N,N-dimethylformamide (DMF). The mixture was ultrasonicated to ensure complete dissolution, forming a clear solution. The vial was then placed in an oven at 80 °C for 1 h. After cooling to room temperature, 25 mg of M-TCPP was added, and the mixture was ultrasonicated again to obtain a clear solution. The vial was subsequently heated in an oven at 90 °C for 48 h. After cooling to room temperature, the product was collected by centrifugation. The precipitate was washed three times with fresh DMF, soaked in acetone for 12 h and washed three additional times, and then dried under vacuum at 60 °C for 1 h to obtain NU-902(M). To remove residual benzoate esters, NU-902(M) was dispersed in a mixture of 1 mL of 4 M HCl and 9 mL of DMF and heated in an oven at 100 °C for 12 h. After cooling to room temperature, the product was collected by centrifugation, washed three times with DMF and acetone, and finally dried under vacuum at 60 °C for 1 h to obtain the activated NU-902(M).

3 Results and discussion

3.1 Material characterization

FT-IR spectroscopy confirms the structural evolution from the precursors to the MOFs (Fig. 1(b) and Fig. S1 in the Electronic Supplementary Material (ESM)). For the porphyrin precursor TMCP, the characteristic absorption peaks at 1724 cm^{-1} (ν(C=O)) and 1275 cm^{-1} (ν(C–O)) confirm the successful introduction of methoxycarbonyl groups, while the absorption peak at 1606 cm^{-1} (porphyrin ring ν(C=C)), bands in the 700–900 cm^{-1} range (ν(C–H)), and the peak at 3318 cm^{-1} (ν(N–H)) are consistent with previous reports [44]. Upon metallation to form M-TCPP (illustrated by Fe-TCPP), the emergence of carboxylate signatures at 1695 cm^{-1} ($\nu_{as}(COO^-)$) and 1398 cm^{-1} ($\nu_s(COO^-)$), together with the disappearance of the ν(N–H) band at 3318 cm^{-1} and the appearance of a new band at approximately 1000 cm^{-1} corresponding to ν(M–N), confirm successful coordination of the transition metal at the porphyrin core. For the assembled NU-902(M) series, complete deprotonation of the carboxylate ligands and their bidentate coordination with the metal nodes lead to a pronounced redshift of the ν(C=O) band to around 1600 cm^{-1}, accompanied by a slight blueshift of the ν(O–H) band to approximately 1414 cm^{-1}. Together with the presence of the ν(M–N) vibration at about 1000 cm^{-1}, these features confirm the structural integrity of the ligands during framework assembly. Newly assigned Zr–O vibration bands in the 400–700 cm^{-1} region provide direct evidence for coordination of the Zr nodes. Moreover, the nearly identical FT-IR spectra observed for the Fe-, Co-, Ni-, and Cu-based analogs (Fig. S1 in the ESM) further demonstrate the structural consistency of the NU-902(M = Fe, Co, Ni, Cu) series [45].

PXRD analysis further verifies the phase purity and structural

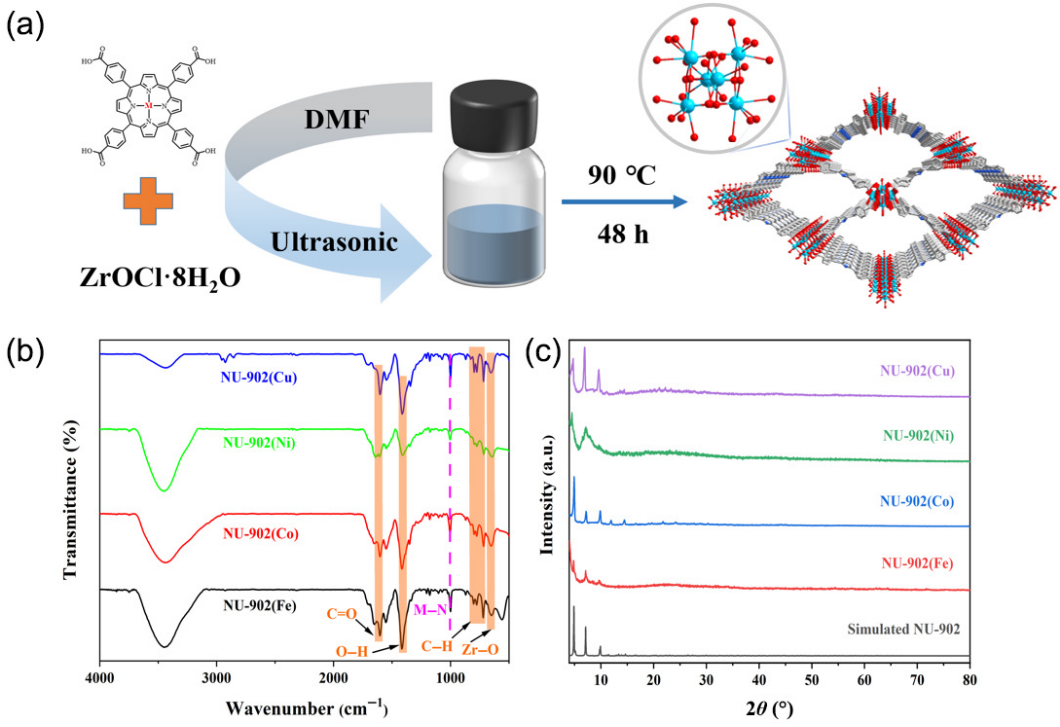

Figure 1 (a) Preparation flow chart of NU-902(M). (b) FT-IR spectra of NU-902(M). (c) PXRD spectra of NU-902(M).

integrity of NU-902(M) (M = Fe, Co, Ni, Cu) (Fig. 1(c)). The NU-902(Fe), NU-902(Co), NU-902(Ni), and NU-902(Cu) samples exhibit three characteristic diffraction peaks at $2\theta = 4.85°$, 7.10°, and 9.80°, which agree well with the simulated diffraction pattern of NU-902 and show no additional impurity peaks [46]. This result indicates high phase purity and successful retention of the parent framework topology after transition-metal substitution.

SEM reveals pronounced metal-dependent morphological evolution in NU-902(M). As shown in Fig. S2 in the ESM, NU-902(Fe) and NU-902(Co) exhibit uniform spindle-shaped crystals with dimensions of approximately 1.5 μm × 700 nm and 2.8 μm × 1.0 μm, respectively. In contrast, NU-902(Ni) forms nearly spherical particles with an average diameter of about 300 nm, whereas NU-902(Cu) displays a capsule-like morphology with distinctive aspect ratios and curvatures, measuring approximately 4.0 μm in length and 2.0 μm in diameter. These observations indicate that the nature of the transition metal plays a significant role in regulating the crystal shape and size of NU-902 materials. The observed morphological and dimensional variations are likely associated with differences in coordination behavior, crystallization dynamics, and lattice regulation effects induced by different metal ions, leading to distinct morphologies within the same NU-902 topology [47].

TEM coupled with energy-dispersive X-ray spectroscopy mapping was employed to further elucidate the microstructure and elemental distribution of the samples. As shown in Fig. 2, the TEM images confirm morphological features consistent with the SEM observations. The elemental mapping results demonstrate that C, N, O, Zr, and the corresponding transition metals (Fe, Co, Ni, and Cu) are uniformly distributed throughout the samples. This uniform distribution confirms that the transition metals successfully replace the N–H sites in the porphyrin ligands and are homogeneously incorporated into the MOF framework. The pore structure of NU-902(Cu) was further investigated by nitrogen adsorption–desorption isotherm measurements (Fig. S3 in the ESM). The pristine NU-902(Cu) exhibits a Brunauer–Emmett–Teller (BET) specific surface area of 1208.73 $m^2 \cdot g^{-1}$ and displays a typical type I isotherm, indicating a three-dimensional interconnected pore network dominated by micropores (< 2 nm).

XPS was used to analyze the chemical states and coordination environments of the NU-902(M) series (M = Fe, Co, Ni, Cu). Survey spectra (Fig. 3(a)) confirm the elemental composition of all samples through the presence of characteristic N 1s, M 2p (M = Fe, Co, Ni, Cu), C 1s, O 1s, and Zr 3d signals. High-resolution C 1s spectra (Figs. S4(a), S5(a), S6(a), and S7(a) in the ESM) display three distinct peaks at binding energies of 284.80 eV, corresponding to aromatic C–C/C–H, 286.26 eV, assigned to C–O species from $-OCH_3$/–COOH groups, and 288.92 eV, attributed to carboxyl C=O [48], confirming successful ligand incorporation. The N 1s spectra (Fig. 3(b)) exhibit peaks at 398.66 and 399.72 eV, assigned to pyrrolic and pyridinic nitrogen, respectively, confirming the porphyrinic nitrogen environment. In addition, M–N coordination bonds are evidenced by peaks at 401.50 eV for Fe, 401.99 eV for Co, 401.58 eV for Ni, and 401.50 eV for Cu, demonstrating successful metallation of the porphyrin centers. The O 1s spectra (Figs. S4(b), S5(b), S6(b), and S7(b) in the ESM), taking NU-902(Cu) as an example, show contributions at 532.06 eV, corresponding to Zr–O clusters, and 534.14 eV, assigned to carboxyl C=O, indicating intact connectivity between the Zr clusters and organic ligands. The Zr 3d spectra (Figs. S4(c), S5(c), S6(c), and S7(c) in the ESM), taking NU-902(Cu) as an example, exhibit doublets at 183.06 eV ($3d_{5/2}$) and 185.45 eV ($3d_{3/2}$), consistently indicating a Zr^{4+} oxidation state [49]. Analysis of the transition-metal 2p spectra reveals distinct oxidation behaviors. The Fe 2p spectrum (Fig. 3(c)) shows the coexistence of Fe^{2+} species at 711.33 eV ($2p_{3/2}$) and 724.46 eV ($2p_{1/2}$) and Fe^{3+} species at 713.65 eV ($2p_{3/2}$) and 726.43 eV ($2p_{1/2}$) [50], which can be attributed to ligand field effects of the porphyrin framework or partial oxidation during activation. Similarly, the Co 2p spectrum (Fig. 3(d)) reveals mixed Co^{2+} states at 781.74 eV ($2p_{3/2}$) and 796.69

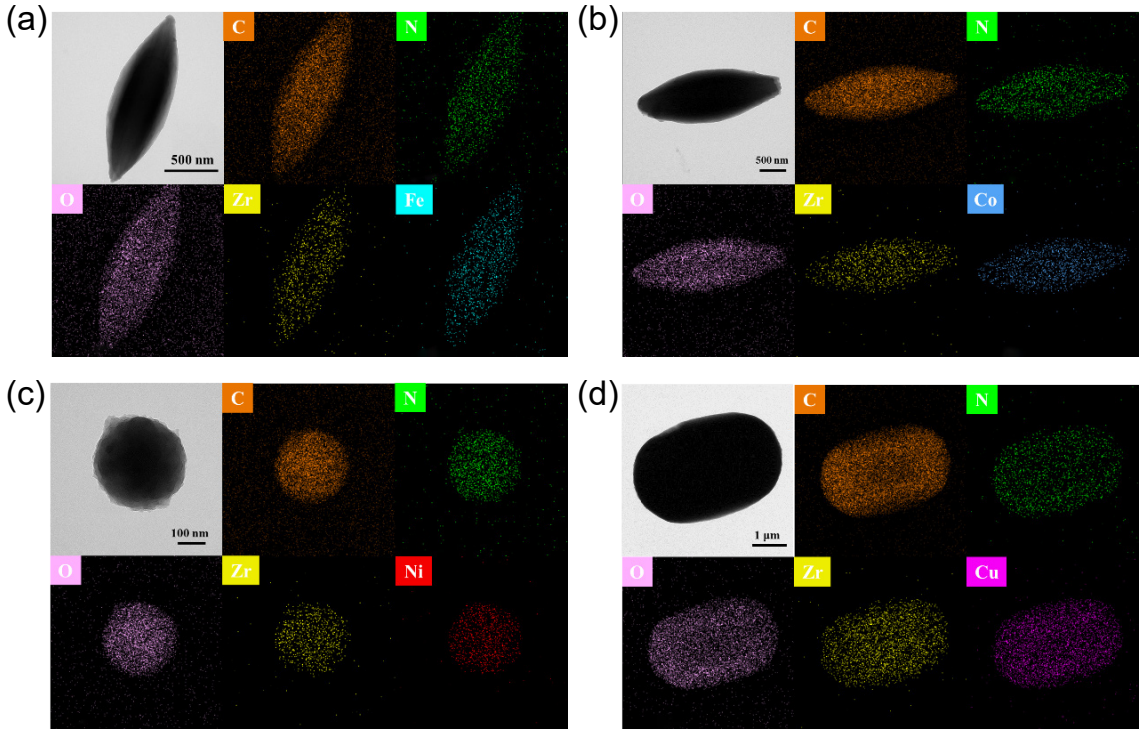

Figure 2 TEM images and elemental distribution of (a) NU-902(Fe), (b) NU-902(Co), (c) NU-902(Ni), and (d) NU-902(Cu).

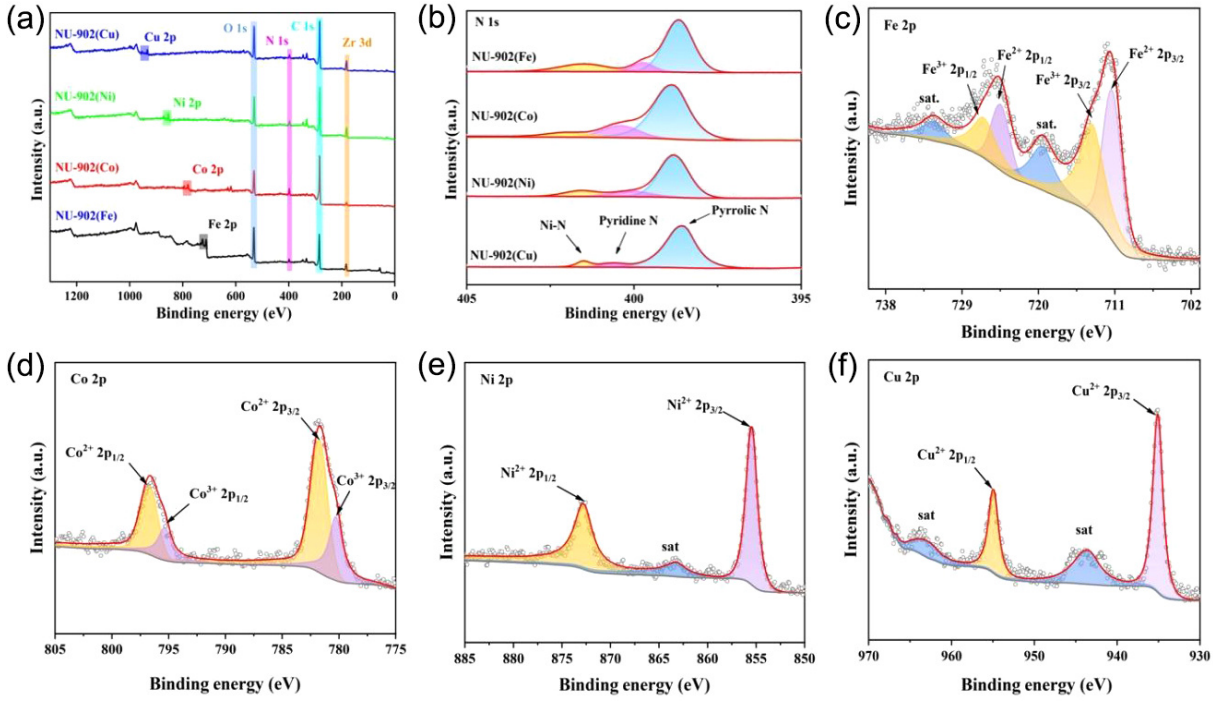

Figure 3 (a) XPS full spectra, (b) N 1s fine spectra of NU-902(M), (c) Fe 2p fine spectrum of NU-902(Fe), (d) Co 2p fine spectrum of NU-902(Co), (e) Ni 2p fine spectrum of NU-902(Ni), and (f) Cu 2p fine spectrum of NU-902(Cu).

eV ($2p_{1/2}$) and Co^{3+} states at 780.28 eV ($2p_{3/2}$) and 795.35 eV ($2p_{1/2}$) [50, 51]. In contrast, the Ni 2p spectrum (Fig. 3(e)) exhibits characteristic peaks at 855.43 eV ($2p_{3/2}$) and 872.79 eV ($2p_{1/2}$), together with a satellite peak at 863.38 eV, confirming the presence of Ni^{2+} [52]. The Cu 2p spectrum (Fig. 3(f)) displays peaks at 935.06 eV ($2p_{3/2}$) and 954.91 eV ($2p_{1/2}$), accompanied by shake-up satellite features at 943.88 and 963.28 eV, verifying the +2 valence state of Cu [53]. Notably, the characteristic peaks of Fe^{3+} and Cu^{2+} shift toward higher binding energies, indicating a downshift of their d-band centers. In contrast, the characteristic peaks of Co^{2+}, Co^{3+}, and Fe^{2+} show no significant shifts, suggesting negligible changes in their d-band centers. A downshifted d-band center weakens H^* adsorption, thereby suppressing the competing hydrogen evolution reaction and favoring the nitrate reduction reaction [54, 55].

3.2 Electrochemical performance measurements

The electrocatalytic nitrate-to-ammonia conversion performance of the NU-902(M) catalysts was systematically evaluated in a standard three-electrode H-type cell using a neutral electrolyte (0.1 M Na_2SO_4, pH = 7.0) [56]. LSV curves of NU-902(M) recorded in nitrate-containing and nitrate-free electrolytes are shown in Fig. S8 in the ESM. The current density in the presence of nitrate is approximately 2–3 times higher at −0.8 V vs. RHE, confirming the intrinsic activity of the catalysts toward nitrate reduction.

Constant-potential electrolysis of NU-902(M) catalysts was conducted over the potential range from −0.6 to −1.0 V vs. RHE in a neutral electrolyte containing 0.1 M Na_2SO_4 and 0.1 M $NaNO_3$. The chronoamperometric profiles (Fig. 4(b), and Figs. S12(a), S13(a), and S14(a) in the ESM) reveal a pronounced increase in cathodic current density with increasingly negative applied potentials. Quantitative analysis of the reaction products was performed using ultraviolet–visible (UV–vis) spectroscopy. Figures 4(b) and 4(c) display the colorimetric absorbance profiles of NH_3 and NO_2^- during the nitrate reduction reaction catalyzed by NU-902(Cu). The ammonia yield and FE were calculated based on calibration curves obtained from UV–vis absorption spectra of NH_4Cl at different concentrations (Fig. S9 in the ESM). Comparative evaluation of the electrocatalytic nitrate reduction performance, including ammonia yield (Fig. 4(e)) and ammonia FE (Fig. 4(f)), confirms the effectiveness of NU-902(M) catalysts for nitrate-to-ammonia conversion. Within the low-overpotential region, the FE for ammonia increases markedly with increasingly negative potentials, which is attributed to enhanced multielectron transfer during the eight-electron reduction process and strong potential-driven effects. At more negative potentials, a decline in FE is observed due to intensified competition from the hydrogen evolution reaction. Notably, NU-902(Cu) exhibits superior performance compared with NU-902(Fe), NU-902(Co), and NU-902(Ni) (Fig. S11 in the ESM). The comparative electrocatalytic nitrate reduction performance of the NU-902(M) series is summarized in Table 1, highlighting the strong dependence of catalytic activity on the incorporated metal center. NU-902(Fe) achieves optimal performance at −0.9 V vs. RHE, delivering an ammonia yield of 14.01 $mg{\cdot}h^{-1}{\cdot}mg_{cat.}^{-1}$ with a FE of 63.83%. NU-902(Co) shows its highest activity at −0.8 V vs. RHE, with an ammonia yield of 9.51 $mg{\cdot}h^{-1}{\cdot}mg_{cat.}^{-1}$ and a FE of 71.51%. NU-902(Ni) performs best at −0.7 V vs. RHE, producing 2.40 $mg{\cdot}h^{-1}{\cdot}mg_{cat.}^{-1}$ with a FE of 67.99%. Among all catalysts, NU-902(Cu) demonstrates the best overall performance at −0.9 V vs. RHE, achieving an ammonia yield of 13.76 $mg{\cdot}h^{-1}{\cdot}mg_{cat.}^{-1}$ and an FE of 71.65%. Comprehensive analysis further reveals that NU-902(Cu) generates the lowest amounts of NO_2^- and H_2 by-products while maintaining the highest ammonia FE, indicating its superior selectivity and catalytic efficiency. Moreover, comparison with

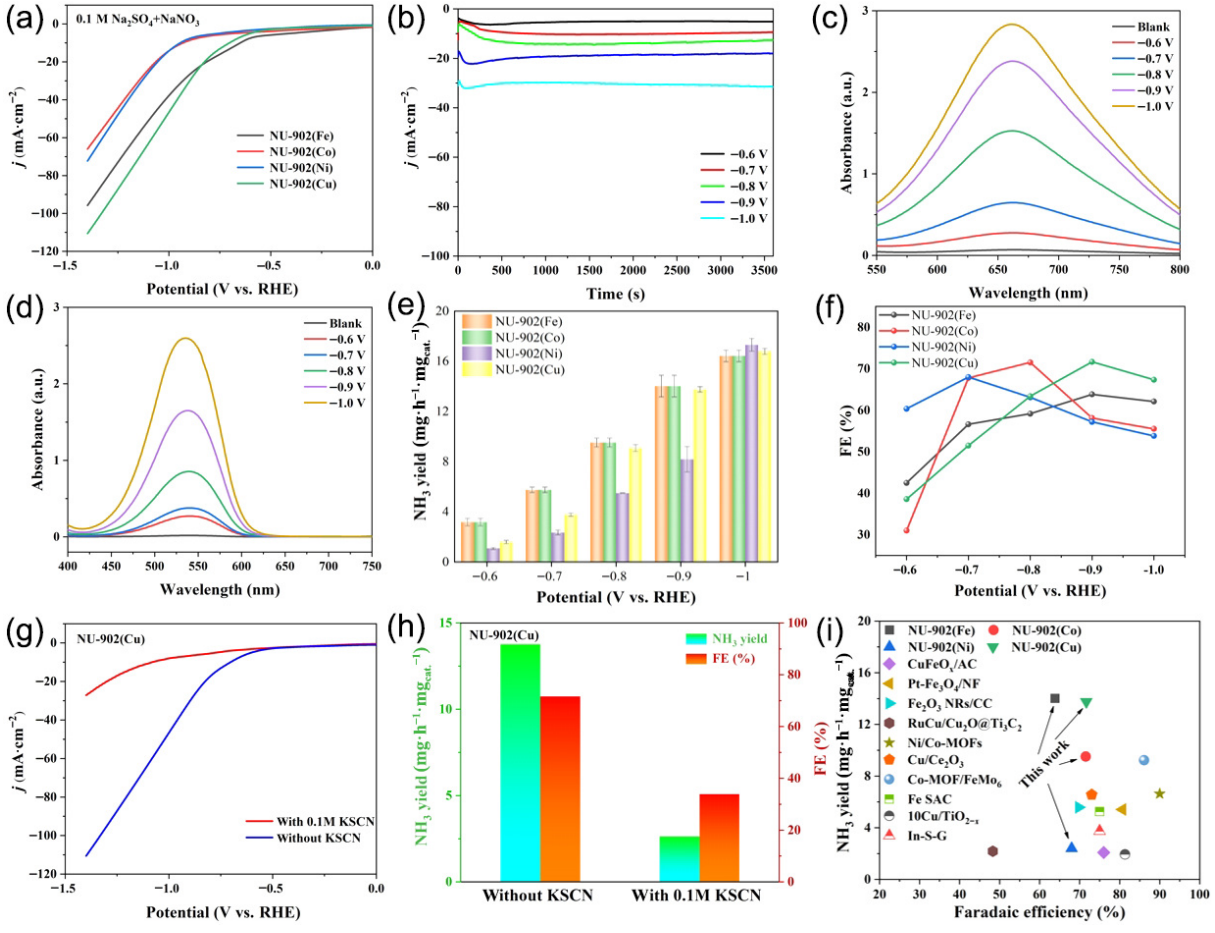

Figure 4 (a) LSV curves of NU-902(M) in nitrate electrolyte. (b) Time–current curves of NU-902(Cu) at −0.6 to −1.0 V vs. RHE. (c) UV–vis spectra of NH_3. (d) UV–vis spectra of NO_2^-. (e) Electrochemical nitrate ammonia yield comparison of NU-902(M). (f) Faradic efficiency comparison of electrochemical nitrate ammonia yield in NU-902(M). (g) LSV curves of NU-902(Cu) with/without KSCN electrolyte. (h) NH_3 yield and Faradic efficiency of NU-902(Cu) with/without KSCN electrolyte. (i) NU-902(M) and some recently reported performance comparisons of electrocatalysts in neutral electrolytes.

Table 1 The optimal catalytic performance of NU-902(M) for e-NO_3RR

Catalyst	Voltage (V vs. RHE)	NH_3 yield ($mg \cdot h^{-1} \cdot mg_{cat.}^{-1}$)	FE (%)
NU-902(Fe)	-0.9	14.01	63.83
NU-902(Co)	-0.8	9.51	71.51
NU-902(Ni)	-0.7	2.40	67.99
NU-902(Cu)	-0.9	13.76	71.65

recently reported electrocatalysts (Fig. 4(i) and Table S5 in the ESM) shows that NU-902(Cu) outperforms most catalysts of the same class, underscoring its strong potential for practical applications in electrocatalytic nitrate reduction.

To elucidate the nature of the catalytic active centers, catalyst poisoning experiments were conducted by introducing 0.1 M KSCN into the electrolyte containing 0.1 M $NaNO_3$ and 0.1 M Na_2SO_4. The SCN^- ions selectively coordinate with single-metal M sites through strong binding interactions, thereby blocking reactant adsorption at the active centers. Electrochemical measurements show that, compared with the control experiments, the introduction of KSCN leads to a pronounced decrease in cathodic current density, ammonia yield, and FE (Figs. 4(g) and 4(h), and Fig. S15 in the ESM). These results systematically illustrate the changes in key electrochemical metrics, particularly ammonia FE, before and after the addition of KSCN, which serves as a specific poison for M–N_4 sites. Similar to NU-902(Cu), the Fe-, Co-, and Ni-based samples all exhibit a substantial decline in ammonia FE after KSCN addition, for example, decreasing from an initial value of 63.0% to 28.2%. The consistent trends observed across all metal-substituted samples strongly confirm that M–N_4 moieties act as the universal active centers for nitrate reduction in the NU-902(M) series, rather than being unique to the Cu-based catalyst.

The electrochemical active surface area (ECSA) of the NU-902(M) series was evaluated using cyclic voltammetry, with measurements conducted in the potential window of 0.1–0.2 V vs. RHE at scan rates ranging from 10 to 90 $mV \cdot s^{-1}$. Quantitative analysis based on the double-layer capacitance (C_{dl}) values (Figs. 5(a)–5(e)) reveals distinct differences in the ECSA among the various metal-substituted materials. The C_{dl} values follow the order NU-902(Cu) (2.32 $mF \cdot cm^{-2}$) > NU-902(Fe) (2.24 $mF \cdot cm^{-2}$) > NU-902(Co) (1.85 $mF \cdot cm^{-2}$) > NU-902(Ni) (1.74 $mF \cdot cm^{-2}$) (Table S1 in the ESM). Notably, the C_{dl} value of NU-902(Cu) is 33.3% higher than that of the Ni-based material, consistent with its higher current density and superior electrocatalytic nitrate reduction (e-NO_3RR) performance observed in the LSV measurements. These results indicate that NU-902(Cu) possesses a larger ECSA. Moreover, its ECSA-normalized specific activity is second only to that of NU-902(Fe), suggesting a high density of exposed active sites. This characteristic effectively accelerates the kinetics of the nitrate reduction reaction and provides a microstructural explanation for the superior catalytic performance of NU-902(Cu) [57]. The charge transport properties of the NU-902(M) catalysts were further investigated using EIS (Fig. 5(f)). The charge-transfer resistance (R_{ct}) and solution resistance (R_s) values for all NU-902(M) samples were obtained through equivalent circuit fitting (Table S2 in the ESM). Analysis of the Warburg impedance in the low-frequency region shows that NU-902(Cu) exhibits the steepest linear slope, indicating the lowest ion diffusion resistance and more efficient electron transport. Combined with its relatively high double-layer capacitance value (C_{dl} = 2.32 $mF \cdot cm^{-2}$), NU-902(Cu) demonstrates an enhanced ECSA compared with the other materials, reflecting a higher exposure of active sites. These features are consistent with its superior e-NO_3RR performance and indicate that Cu substitution achieves a synergistic effect of high intrinsic activity and rapid electron transport.

Based on these advantages, subsequent investigations focused on NU-902(Cu) for control experiments and stability evaluations. To identify the nitrogen source for electrocatalytic ammonia synthesis, three sets of control experiments were designed and systematically verified using UV–vis absorption spectroscopy and ^1H nuclear magnetic resonance (NMR) analysis. (1) In an electrolyte

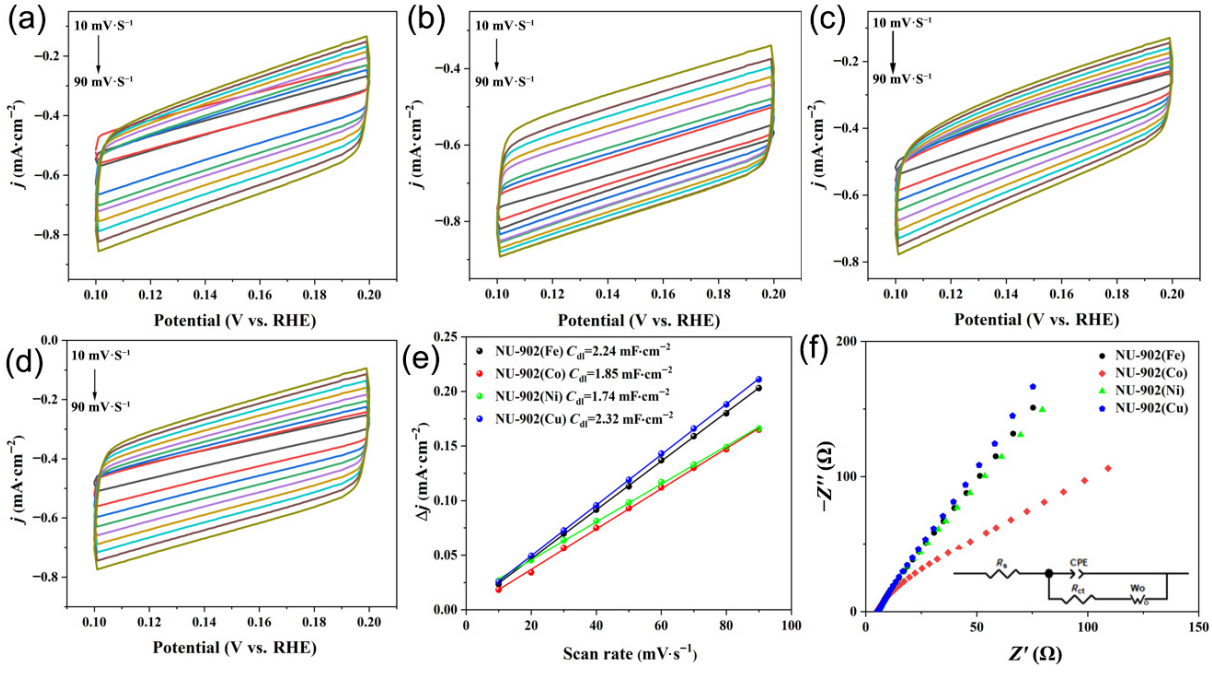

Figure 5 Electrochemical active area (EA) of (a) NU-902(Fe), (b) NU-902(Co), (c) NU-902(Ni), and (d) NU-902(Cu). (e) Double layer capacitance (C_{dl}) test of NU-902(M). (f) EIS analysis of NU-902(M).

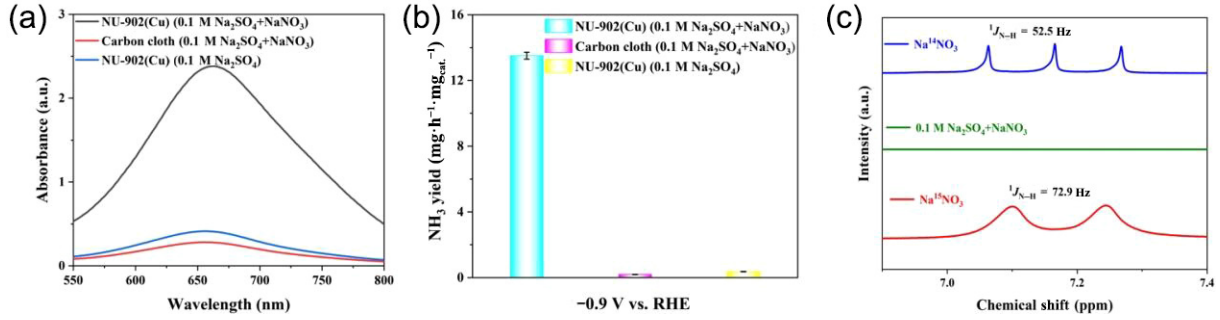

Figure 6 (a) UV–vis spectra of NU-902(Cu) in electrolyte containing or not containing nitrate and UV–vis spectrum of blank carbon cloth in electrolyte containing nitrate. (b) The ammonia yields of NU-902(Cu) in electrolyte containing or not containing nitrate and the ammonia yield of blank carbon cloth in electrolyte containing nitrate. (c) ^{1}H NMR spectra of the electrolyte after 1 h electrocatalytic testing using $^{14}NO_3^-$ and $^{15}NO_3^-$ as N sources with NU-902(Cu).

containing 0.1 M $NaNO_3$ and 0.1 M Na_2SO_4, constant-potential electrolysis was performed using bare carbon cloth as the working electrode at −0.9 V vs. RHE for 1 h. The UV–vis spectrum (Fig. 6(a)) showed no discernible characteristic absorption peak at 652 nm, and the corresponding ammonia yield was extremely low (0.19 $mg{\cdot}h^{-1}{\cdot}mg_{cat.}^{-1}$) (Fig. 6(b)). These results exclude contributions from the electrode substrate or electrolyte impurities to ammonia formation. (2) Using NU-902(Cu) as the working electrode, electrolysis was carried out under identical conditions in a nitrate-free 0.1 M Na_2SO_4 electrolyte. No characteristic NH_3 signals were observed in the UV–vis spectra (Fig. 6(a)), and the ammonia yield was only 0.36 $mg{\cdot}h^{-1}{\cdot}mg_{cat.}^{-1}$, indicating that ammonia production strictly depends on the presence of NO_3^- in the electrolyte rather than on decomposition of nitrogen-containing species within the catalyst. (3) To directly trace the nitrogen source, ^{15}N isotope-labeling experiments were conducted using $Na^{14}NO_3$ and $Na^{15}NO_3$ as nitrogen sources for e-NO_3RR tests (Fig. 6(c)). ^{1}H NMR analysis revealed that when $^{14}NO_3^-$ was used, characteristic triplet peaks of $^{14}NH_4^+$ appeared at δ = 7.07, 7.17, and 7.27 ppm (J = 52.5 Hz). In contrast, when $^{15}NO_3^-$ was employed, characteristic doublet peaks of $^{15}NH_4^+$ were observed at δ = 7.11 and 7.25 ppm (J = 72.9 Hz), consistent with the ^{15}N–^{1}H coupling effect. Notably, the ^{1}H NMR spectrum of the unreacted electrolyte exhibited none of these characteristic peaks, ruling out the possibility of environmental nitrogen contamination. Collectively, these results confirm that NO_3^- in the electrolyte is the sole nitrogen source for NH_3 formation.

In situ FT-IR spectroscopy was employed to monitor reactant consumption and the reaction environment of NU-902(Cu) during nitrate reduction. As shown in Figs. 7(a) and 7(b), absorption bands at 1212, 1420, 1455, and 1540 cm^{-1}, corresponding to *NH, *NH_2, NH_4^+, and symmetric N–O vibrations, respectively, indicate the formation of NH_4^+ and the depletion of N–O species during the reaction [58]. With increasingly negative applied potentials, the intensity associated with NH_4^+ formation increases, demonstrating enhanced ammonia production. In Fig. 7(b), the infrared band at 1362 cm^{-1}, attributed to the asymmetric N–O stretching vibration of NO_3^-, reflects the activation and consumption of nitrate catalyzed by NU-902(Cu) under applied potential [59, 60]. In addition, a band at 1560 cm^{-1} corresponds to the antisymmetric N–O stretching vibration of NO_2^-, confirming NO_2^- as a reaction intermediate, which is consistent with the electrochemical results. Based on the *in situ* FT-IR analysis, the nitrate reduction pathway on the NU-902(Cu) surface is proposed as follows: NO_3^- → *NO_2 → *NO → *NH → *NH_2 → NH_4^+. These *in situ* FT-IR observations confirm the successful electrocatalytic conversion of nitrate to ammonia over NU-902(Cu) in this study.

The stability of a catalyst is a critical index for evaluating its potential practical application [61]. Herein, NU-902(Cu) was systematically assessed through electrochemical and structural stability analyses. (1) Electrochemical stability was evaluated using two complementary approaches. Cyclic stability tests consisting of six consecutive e-NO_3RR cycles at −0.9 V vs. RHE (Figs. 8(a) and 8(b)) demonstrate robust performance, with current density fluctuations confined within ±5%, while the ammonia yield and FE remained stable, with minimum values of 12.35 $mg{\cdot}h^{-1}{\cdot}mg_{cat.}^{-1}$ and 69.01%, respectively, confirming excellent cycling durability. In addition, long-term electrolysis conducted at −0.9 V vs. RHE for 12 h (Fig. 8(c)) shows that the current density of NU-902(Cu) retains approximately 90% of its initial value, corresponding to only

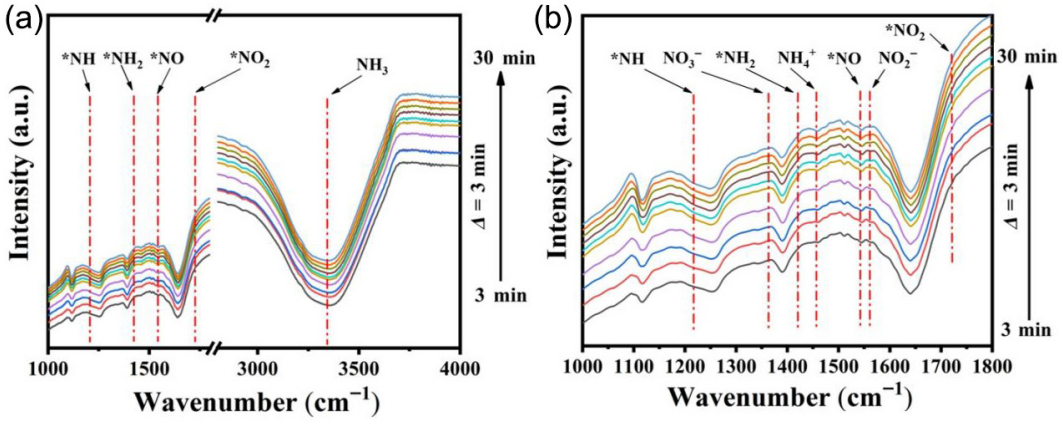

Figure 7 *In situ* FT-IR spectra of electrocatalytic NO_3RR on NU-902(Cu) at different times: (a) in 1000–4000 cm^{-1} and (b) in 1000–1800 cm^{-1} wavenumber range.

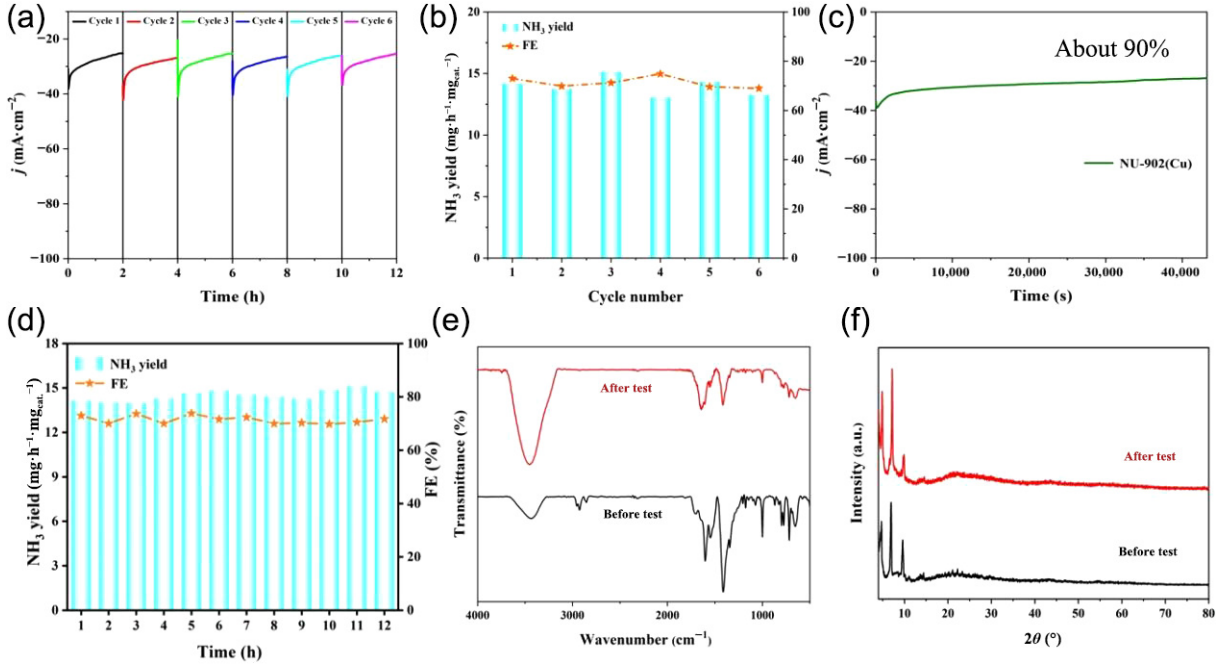

Figure 8 (a) *i–t* curves of NU-902(Cu) after 6 cycles. (b) NH_3 yield and FE of NU-902(Cu) after 6 cycles. (c) *i–t* curves of NU-902(Cu) at −0.9 V vs. RHE for 12 h. (d) NH_3 yield and FE per hour constant-potential electrolysis at −0.9 V vs. RHE during 12 h. (e) FT-IR spectra of NU-902(Cu) before and after cyclic testing. (f) PXRD spectra of NU-902(Cu) before and after cyclic testing.

a minor 10% decay. The ammonia yield and FE monitored at hourly intervals (Fig. 8(d)) also remain stable, further demonstrating the long-term operational stability of the catalyst. (2) Structural stability was investigated by postreaction FT-IR, PXRD, and XPS analyses. The FT-IR spectrum obtained after cycling (Fig. 8(e)) exhibits complete retention of all characteristic absorption bands without peak shifts or intensity attenuation, indicating the absence of ligand decomposition or desorption. The PXRD patterns recorded after stability testing (Fig. 8(f)) maintain excellent agreement with the original diffraction peaks at $2\theta = 4.85°$, 7.10°, and 9.80°, with no detectable impurity phases, unequivocally confirming preservation of the crystalline framework. Furthermore, XPS spectra collected after catalysis (Fig. S16 in the ESM) show no significant differences from those obtained before electrolysis, with consistent binding energies for all elements, providing additional evidence for the structural robustness of the material. Collectively, these results demonstrate that NU-902(Cu) maintains both high electrochemical performance and structural integrity under prolonged electrocatalytic conditions.

4 Conclusion

In this work, a series of NU-902(M) catalysts (M = Cu, Fe, Co, Ni) were fabricated via an *in situ* metal substitution strategy, yielding an efficient electrocatalytic system for nitrate reduction with high activity and long-term cycling stability. Based on *in situ* FT-IR analysis, the nitrate reduction pathway on the NU-902(Cu) surface is proposed as $NO_3^- \rightarrow {}^*NO_2 \rightarrow {}^*NO \rightarrow {}^*NH \rightarrow NH_2 \rightarrow NH_4^+$. The NU-902(M) materials exhibit several distinctive features. First, the rigid MOF backbone constructed from zirconium–oxo clusters ensures excellent stability in aqueous environments. Second, the metal–N_4 coordination structure formed by porphyrin ligands coordinated to transition metal centers facilitates the adsorption of NO_3^- and reaction intermediates, thereby optimizing the kinetics of the eight-electron-transfer pathway. Third, in the case of NU-902(Cu), its superior catalytic performance originates from the downshifted d-band center of Cu, as evidenced by the Cu $2p_{3/2}$ binding energy at 935.06 eV, which weakens H adsorption and suppresses the competing hydrogen evolution reaction. This effect, combined with the largest ECSA = 2.32 mF·cm^{-2} and the lowest charge-transfer resistance among the studied catalysts, enables efficient mass transport and electron–proton coupling. As a result, NU-902(Cu) achieves an ammonia yield rate of 13.76 mg·h^{-1}·mg$^{-1}_{cat.}$ with an FE of 71.65% at −0.9 V vs. RHE. These results demonstrate that NU-902(Cu) outperforms most previously reported catalysts of the same class, highlighting its strong potential for practical applications in electrocatalytic nitrate reduction.

Electronic Supplementary Material: Supplementary material (experimental details, detection method, structural characterization diagram, performance test diagram etc.) is available in the online version of this article at https://doi.org/10.26599/POM.2026.9140116.

Data availability

All data needed to support the conclusions in the paper are presented in the manuscript and the Electronic Supplementary Material. Additional data related to this paper may be requested from the corresponding author upon request.

Acknowledgements

This work was supported by the National Natural Science Foundation of China (Nos. 32541097 and 22171059), Shandong Provincial Natural Science Foundation (No. ZR2022MB096), Heilongjiang Provincial Natural Science Foundation of China (No. LH2024B015), and Heilongjiang Provincial Science and Technology Innovation Base Award Program (No. JD25A023).

Declaration of competing interest

The authors have no competing interests to declare that are relevant to the content of this article.

Author contribution statement

L. Q. L.: Data curation, project administration, validation, writing manuscript, experimental design. X. M. W.: Data curation, project administration, validation, experimental design. J. L.: Project administration, writing manuscript. Y. F. W.: Project administration, funding acquisition. H. J. P.: Project administration, funding acquisition, writing manuscript. H. Y. M: Project administration, funding acquisition. All the authors have approved the final manuscript.

Use of AI statement

None.

References

[1] Jiang, H. X.; Li, T. Y.; Gao, Y. T.; Fan, J. P.; Gan, D. W.; Yuan, S.; Hong, L. F.; Feng, Y.; Sun, J.; Song, Q. et al. Sustainable ammonia synthesis: Opportunities for electrocatalytic nitrate reduction. *J. Energy Chem.* **2025**, *105*, 630–668.

[2] Wang, X. M.; Jiang, Q. S.; Rong, S.; Li, H. Y.; Zhao, N.; Pang, H. J.; Ma, H. Y. Orchestrated electron transfer in reduced polyoxometalate-based coordination architectures for facilitating nitrate-to-ammonia electrosynthesis. *J. Colloid Interface Sci.* **2025**, *694*, 137717.

[3] Zheng, X. N.; Yan, Y.; Li, X. X.; Liu, Y.; Yao, Y. Theoretical insights into dissociative-associative mechanism for enhanced electrochemical nitrate reduction to ammonia. *J. Hazard. Mater.* **2023**, *446*, 130679.

[4] Yang, X.; Cui, D. H.; Zhang, T. T.; Liu, Y.; Li, F. Y. LSPR-enhanced photocatalytic N_2 fixation over Z-scheme POMOF-derived Cu/WO_2 modified C-BiOBr with multiple active sites. *Inorg. Chem. Front.* **2024**, *11*, 8246–8257.

[5] Zhang, R.; Zhang, Y. Q.; Xiao, B.; Zhang, S. C.; Wang, Y. B.; Cui, H. L.; Li, C.; Hou, Y.; Guo, Y.; Yang, T. et al. Phase engineering of high-entropy alloy for enhanced electrocatalytic nitrate reduction to ammonia. *Angew. Chem., Int. Ed.* **2024**, *63*, e202407589.

[6] Feng, Z. M.; Li, G.; Wang, X. M.; Gómez-García, C. J.; Xin, J. J.; Ma, H. Y.; Pang, H. J.; Gao, K. Q. FeS_2/MoS_2@RGO hybrid materials derived from polyoxomolybdate-based metal-organic frameworks as high-performance electrocatalyst for ammonia synthesis under ambient conditions. *Chem. Eng. J.* **2022**, *445*, 136797.

[7] Zang, D. J.; Wang, H. Q. Polyoxometalate-based nanostructures for electrocatalytic and photocatalytic CO_2 reduction. *Polyoxometalates* **2022**, *1*, 9140006.

[8] Zang, D. J.; Gao, X. J.; Li, L. Y.; Wei, Y. G.; Wang, H. Q. Confined interface engineering of self-supported Cu@N-doped graphene for electrocatalytic CO_2 reduction with enhanced selectivity towards ethanol. *Nano Res.* **2022**, *15*, 8872–8879.

[9] Hao, D.; Chen, Z. G.; Figiela, M.; Stepniak, I.; Wei, W.; Ni, B. J. Emerging alternative for artificial ammonia synthesis through catalytic nitrate reduction. *J. Mater. Sci. Technol.* **2021**, *77*, 163–168.

[10] Wang, X. M.; Yang, M. L.; Gómez-García, C. J.; Cao, X. X.; Jin, Z. X.; Ma, H. Y.; Pang, H. J.; Yang, G. X. Phase-regulated $FeSe_2$@(1T-2H)-$MoSe_2$ derived from anderson-type polyoxometalate as an efficient electrocatalyst for the nitrogen reduction reaction. *ACS Sustain. Chem. Eng.* **2025**, *13*, 1708–1718.

[11] Sun, J. J.; Li, X. Y.; Zhao, Q. D.; Liu, B. J. Ultrathin nanoflake-assembled hierarchical BiOBr microflower with highly exposed {001} facets for efficient photocatalytic degradation of gaseous *ortho*-dichlorobenzene. *Appl. Catal. B: Environ.* **2021**, *281*, 119478.

[12] Zhao, Y. J.; Bao, Z. Y.; Bai, X. W.; Xu, P. H.; Shi, X. W.; Wu, Q.; Jia, Y.; Zheng, H. J.; Zheng, L. X. Superior electrocatalytic nitrate-to-ammonia conversion activity on CuCo bimetals in neutral media. *Appl. Catal. B: Environ. Energy* **2024**, *357*, 124294.

[13] Lv, Y.; Ke, S. W.; Gu, Y. M.; Tian, B. L.; Tang, L. Y.; Ran, P.; Zhao, Y.; Ma, J.; Zuo, J. L.; Ding, M. N. Highly efficient electrochemical nitrate reduction to ammonia in strong acid conditions with Fe_2M-trinuclear-cluster metal-organic frameworks. *Angew. Chem., Int. Ed.* **2023**, *62*, e202305246.

[14] Ni, Z. H.; Liu, N.; Zhao, C. H.; Mi, L. W. Hexanuclear nickel-added silicotungstates as high-efficiency electrocatalysts for nitrate reduction to ammonia. *Polyoxometalates* **2024**, *3*, 9140044.

[15] Cui, D. H.; Yang, X.; Liu, Y.; Xiang, Y. X.; Li, F. Y. Carbon nitride with grafted benzothiadiazole as electron acceptor and active site to promote exciton dissociation for metal-free photocatalytic N_2 fixation. *J. Colloid Interface Sci.* **2025**, *686*, 795–806.

[16] Shan, Z.; Sun, Y. T.; Wu, M. M.; Zhou, Y. T.; Wang, J. J.; Chen, S.; Wang, R.; Zhang, G. Metal-porphyrin-based three-dimensional covalent organic frameworks for electrocatalytic nitrogen reduction. *Appl. Catal. B: Environ.* **2024**, *342*, 123418.

[17] Cui, D. H.; Yang, X.; Liu, Y.; Ou, T.; Kong, X. Y.; Zhang, Y. L.; Zhang, J. W.; Li, F. Y. Strategy of constructing D–A structure and accurate active sites over graphitic carbon nitride nanowires for high efficient photocatalytic nitrogen fixation. *J. Colloid Interface Sci.* **2025**, *678*, 955–969.

[18] Ma, A. J.; Gui, J. Z.; Huang, Y. M.; Yu, Y. F. Electrocatalytic coupling of anodic nitrogen oxidation and cathodic nitrate reduction for ammonia synthesis from air and water. *Nano Res.* **2024**, *17*, 7824–7829.

[19] Zhou, Q. Y.; Wang, X. M.; Rong, S.; Li, G.; Pang, H. J.; Ma, H. Y. Anderson-type polyoxometalate/MXene heterostructures for efficient electrochemical nitrate reduction to ammonia. *Appl. Surf. Sci.* **2025**, *708*, 163675.

[20] Xu, H.; Ma, Y. Y.; Chen, J.; Zhang, W. X.; Yang, J. P. Electrocatalytic reduction of nitrate-a step towards a sustainable nitrogen cycle. *Chem. Soc. Rev.* **2022**, *51*, 2710–2758.

[21] Feng, D. M.; Zhou, L. X.; White, T. J.; Cheetham, A. K.; Ma, T. Y.; Wei, F. X. Nanoengineering metal-organic frameworks and derivatives for electrosynthesis of ammonia. *Nano-Micro Lett.* **2023**, *15*, 203.

[22] Zou, Y. Y.; Yan, Y. C.; Xue, Q. S.; Zhang, C. Q.; Bao, T.; Zhang, X. C.; Yuan, L.; Qiao, S. C.; Song, L.; Zou, J. et al. MOF-on-MOF heterostructured electrocatalysts for efficient nitrate reduction to ammonia. *Angew. Chem., Int. Ed.* **2024**, *63*, e202409799.

[23] Van Nguyen, T.; Tekalgne, M.; Le, Q. V.; Tran, C. V.; Ahn, S. H.; Kim, S. Y. Recent progress and strategies of non-noble metal electrocatalysts based on MoS_2/MOF for the hydrogen evolution reaction in water electrolysis: An overview. *Microstructures* **2024**, *4*, 2024046.

[24] Li, H.; Wang, K. C.; Sun, Y. J.; Lollar, C. T.; Li, J. L.; Zhou, H. C. Recent advances in gas storage and separation using metal-organic frameworks. *Mater. Today* **2018**, *21*, 108–121.

[25] Xu, X.; Li, X.; Liu, G. B.; Wei, X. X.; Feng, D. M.; Zhang, L. Rational design of high-flux, eco-friendly, and versatile superhydrophobic/superoleophilic PDMS@ZIF-7/$Cu_3(PO_4)_2$ mesh with self-cleaning property for oil-water mixture and emulsion separation. *Inorg. Chem.* **2023**, *62*, 3260–3270.

[26] Li, H.; Sun, Y.; Yuan, Z. Y.; Zhu, Y. P.; Ma, T. Y. Titanium phosphonate based metal-organic frameworks with hierarchical porosity for enhanced photocatalytic hydrogen evolution. *Angew. Chem., Int. Ed.* **2018**, *57*, 3222–3227.

[27] Shrivastav, V.; Sundriyal, S.; Goel, P.; Kaur, H.; Tuteja, S. K.; Vikrant, K.; Kim, K. H.; Tiwari, U. K.; Deep, A. Metal-organic frameworks (MOFs) and their composites as electrodes for lithium battery applications: Novel means for alternative energy storage. *Coord. Chem. Rev.* **2019**, *393*, 48–78.

[28] Ye, Z. Q.; Jiang, Y.; Li, L.; Wu, F.; Chen, R. J. Rational design of MOF-based materials for next-generation rechargeable batteries. *Nano-Micro Lett.* **2021**, *13*, 203.
[29] Zhu, Y. T.; Yue, K. H.; Xia, C. F.; Zaman, S.; Yang, H.; Wang, X. Y.; Yan, Y.; Xia, B. Y. Recent advances on MOF derivatives for non-noble metal oxygen electrocatalysts in zinc-air batteries. *Nano-Micro Lett.* **2021**, *13*, 137.
[30] Zhang, B.; Zheng, Y. J.; Ma, T.; Yang, C. D.; Peng, Y. F.; Zhou, Z. H.; Zhou, M.; Li, S.; Wang, Y. H.; Cheng, C. Designing MOF nanoarchitectures for electrochemical water splitting. *Adv. Mater.* **2021**, *33*, 2006042.
[31] Ding, X. X.; Yuan, Y. Y.; Zhang, Y. G.; Jiang, Z. G.; Zhan, C. H. Chiral polyoxometalate-cyclodextrin frameworks via Mn-mediated assembly: Enhanced stability and catalytic activity. *Polyoxometalates* **2024**, *3*, 9140046.
[32] Li, C. B.; Ji, Y.; Wang, Y. P.; Liu, C. X.; Chen, Z. Y.; Tang, J. L.; Hong, Y. W.; Li, X.; Zheng, T. T.; Jiang, Q. et al. Applications of metal-organic frameworks and their derivatives in electrochemical CO_2 reduction. *Nano-Micro Lett.* **2023**, *15*, 113.
[33] Yang, M. L.; Wang, X. M.; Gómez-García, C. J.; Jin, Z. X.; Xin, J. J.; Cao, X. X.; Ma, H. Y.; Pang, H. J.; Tan, L. C.; Yang, G. X. et al. Efficient electron transfer from an electron-reservoir polyoxometalate to dual-metal-site metal-organic frameworks for highly efficient electroreduction of nitrogen. *Adv. Funct. Mater.* **2023**, *33*, 2214495.
[34] Zhang, S.; Li, M.; Li, J. C.; Song, Q. N.; Liu, X. High-ammonia selective metal-organic framework-derived Co-doped Fe/Fe_2O_3 catalysts for electrochemical nitrate reduction. *Proc. Natl. Acad. Sci. USA* **2022**, *119*, e2115504119.
[35] Yang, X.; Li, M. H.; Xu, L.; Li, F. Y. Limitation of WO_3 in Zn–Co_3O_4 nanopolyhedra by the pyrolysis of $H_3PW_{12}O_{40}$@BMZIF: Synergistic effect of heterostructure and oxygen vacancies for enhanced nitrogen fixation. *Inorg. Chem.* **2023**, *62*, 8710–8718.
[36] Yang, X.; Cui, D. H.; Liu, Y.; Xiang, Y. X.; Li, F. Y. Construction of dual electron channels and multiple active sites in Co–In/Bi/BiOBr for enhanced photocatalytic ammonia production. *J. Colloid Interface Sci.* **2025**, *695*, 137806.
[37] Gao, W. Y.; Chrzanowski, M.; Ma, S. Q. Metal-metalloporphyrin frameworks: A resurging class of functional materials. *Chem. Soc. Rev.* **2014**, *43*, 5841–5866.
[38] Zhang, L. W.; Shi, X. B.; Zhang, Z. H.; Kuchel, R. P.; Namivandi-Zangeneh, R.; Corrigan, N.; Jung, K.; Liang, K.; Boyer, C. Porphyrinic zirconium metal-organic frameworks (MOFs) as heterogeneous photocatalysts for PET-RAFT polymerization and stereolithography. *Angew. Chem., Int. Ed.* **2021**, *60*, 5489–5496.
[39] Yu, K.; Won, D. I.; Lee, W. I.; Ahn, W. S. Porphyrinic zirconium metal-organic frameworks: Synthesis and applications for adsorption/catalysis. *Korean J. Chem. Eng.* **2021**, *38*, 653–673.
[40] Wu, X.; Liu, Z. G.; Gao, T. Y.; Li, Z. Z.; Song, Z. H.; Tang, J.; Feng, F.; Qu, C. Y.; Yao, F. B.; Tang, C. J. Boosting electrocatalytic reduction of nitrate to ammonia over Co_3O_4 nanosheets with oxygen vacancies. *Metals* **2023**, *13*, 799.
[41] Sanwal, P.; Raza, A.; Miao, Y. X.; Lumbers, B.; Li, G. Advances in coinage metal nanoclusters: From synthesis strategies to electrocatalytic performance. *Polyoxometalates* **2024**, *3*, 9140057.
[42] He, H. M.; Li, H. K.; Zhu, Q. Q.; Li, C. P.; Zhang, Z. H.; Du, M. Hydrophobicity modulation on a ferriporphyrin-based metal-organic framework for enhanced ambient electrocatalytic nitrogen fixation. *Appl. Catal. B: Environ.* **2022**, *316*, 121673.
[43] Wang, Z. C.; Liu, S. S.; Wang, M. F.; Zhang, L. F.; Jiang, Y. Z.; Qian, T.; Xiong, J.; Yang, C. T.; Yan, C. L. *In situ* construction of metal-organic frameworks as smart channels for the effective electrocatalytic reduction of nitrate at ultralow concentrations to ammonia. *ACS Catal.* **2023**, *13*, 9125–9135.
[44] Jiao, L.; Dong, Y. Y.; Xin, X.; Qin, L.; Lv, H. J. Facile integration of Ni-substituted polyoxometalate catalysts into mesoporous light-responsive metal-organic framework for effective photogeneration of hydrogen. *Appl. Catal. B: Environ.* **2021**, *291*, 120091.
[45] Wang, Y. R.; Huang, Q.; He, C. T.; Chen, Y. F.; Liu, J.; Shen, F. C.; Lan, Y. Q. Oriented electron transmission in polyoxometalate-metalloporphyrin organic framework for highly selective electroreduction of CO_2. *Nat. Commun.* **2018**, *9*, 4466.
[46] Gong, X. Y.; Noh, H.; Gianneschi, N. C.; Farha, O. K. Interrogating kinetic versus thermodynamic topologies of metal-organic frameworks via combined transmission electron microscopy and X-ray diffraction analysis. *J. Am. Chem. Soc.* **2019**, *141*, 6146–6151.
[47] Li, G.; Wang, X. M.; Pang, H. J.; Ma, H. Y. Molecular Weaving of mixed-addenda polyoxometalates into MOF nanochannels as electron-buffering reservoirs for enhanced nitrate-to-ammonia electrocatalysis. *Adv. Sci.* **2025**, *0*, e21317.
[48] Niu, X. H.; Liu, Y. Q.; Zhao, R.; Yuan, M.; Wang, Y. W.; Zhang, J. Y.; Li, H. X.; Yang, X.; Wang, K. J. Regulating catalytic oxidation enantiomers behavior by imparting chiral microenvironment in Zr-based metal-organic frameworks. *Small* **2024**, *20*, 2404554.
[49] Hu, X.; Yang, Y.; Li, N.; Huang, C. C.; Zhou, Y. S.; Zhang, L. J.; Zhong, Y. X.; Liu, Y. Q.; Wang, Y. Interface-regulated S-type core-shell PCN-224@TiO_2 heterojunction for visible-light-driven generation of singlet oxygen for selective photooxidation of 2-chloroethyl ethyl sulfide. *J. Colloid Interface Sci.* **2024**, *674*, 791–804.
[50] Liu, Y.; Zhong, X.; Liu, M. T.; Zhao, H. Y.; Wang, Z. X.; Ni, R. T.; Wang, Y. Y.; Yang, J.; Gao, F.; Li, Y. G. et al. Composition-engineered FeCo nanoalloys with lattice expansion and optimized electron structure boosting electrocatalytic nitrate reduction. *Appl. Catal. B: Environ. Energy* **2024**, *355*, 124205.
[51] Luo, H.; Wang, X. M.; Jiang, Q. S.; Li, G.; Ren, X. J.; Pang, H. J.; Ma, H. Y. Architecting cobalt-centered 2D sandwich-type polyoxometalate frameworks for selective electrocatalytic nitrate reduction to ammonia. *Inorg. Chem.* **2025**, *64*, 21054–21066.
[52] Zhou, J.; Wen, M.; Huang, R.; Wu, Q. S.; Luo, Y. X.; Tian, Y. K.; Wei, G. F.; Fu, Y. Q. Regulating active hydrogen adsorbed on grain boundary defects of Nano-nickel for boosting ammonia electrosynthesis from nitrate. *Energy Environ. Sci.* **2023**, *16*, 2611–2620.
[53] Wang, L.; Jin, P. X.; Huang, J. W.; She, H. D.; Wang, Q. Z. Integration of copper(Ⅱ)-porphyrin zirconium metal-organic framework and titanium dioxide to construct Z-scheme system for highly improved photocatalytic CO_2 reduction. *ACS Sustain. Chem. Eng.* **2019**, *7*, 15660–15670.
[54] Liu, G.; Chen, Y. F.; Chen, Y. L.; Shi, Y. Q.; Zhang, M. Y.; Shen, G. D.; Qi, P. F.; Li, J. K.; Ma, D. L.; Yu, F. et al. Indirect electrocatalysis S–N/S–S bond construction by robust polyoxometalate based foams. *Adv. Mater.* **2023**, *35*, 2304716.
[55] Wang, C. H.; Shen, W. J.; Xie, Z. R.; Wang, Y. N.; Ding, Y.; Han, N.; Leung, M. K. H.; Liu, B.; Zhu, Z.; Ng, Y. H. Tailoring the microstructure of B-cation octahedra in halide double perovskites for efficient selective CO_2-to-CO photoreduction. *Adv. Funct. Mater.* **2025**, *35*, 2503074.
[56] Rein, J.; Zacate, S. B.; Mao, K. N.; Lin, S. A tutorial on asymmetric electrocatalysis. *Chem. Soc. Rev.* **2023**, *52*, 8106–8125.
[57] Jiang, Q. S.; Wang, X. M.; Tian, S. J.; Pang, H. J.; Song, Y. B.; Ma, H. Y. Polyoxometalate as hydrogen–electron hub in metal–organic complex for electrocatalytic nitrate reduction to ammonia. *Adv. Sci.* **2025**, *0*, e20543.
[58] Lv, L.; Lu, R. H.; Zhu, J. X.; Yu, R. H.; Zhang, W.; Cui, E. H.; Chen, X. B.; Dai, Y. H.; Cui, L. M.; Li, J. et al. Coordinating the edge defects of bismuth with sulfur for enhanced CO_2 electroreduction to formate. *Angew. Chem.* **2023**, *135*, e202303117.
[59] Song, Z. M.; Liu, Y.; Zhong, Y. Z.; Guo, Q.; Zeng, J.; Geng, Z. G. Efficient electroreduction of nitrate into ammonia at ultralow concentrations via an enrichment effect. *Adv. Mater.* **2022**, *34*, 2204306.
[60] Fang, J. Y.; Zheng, Q. Z.; Lou, Y. Y.; Zhao, K. M.; Hu, S. N.; Li, G.; Akdim, O.; Huang, X. Y.; Sun, S. G. Ampere-level current density

ammonia electrochemical synthesis using CuCo nanosheets simulating nitrite reductase bifunctional nature. *Nat. Commun.* **2022**, *13*, 7899.
[61] Qi, L. J.; Fu, Y.; Ji, B. R.; Sarsenbekuly, B.; Kang, W. L.; Yang, H. B.; Liu, S. J. Bifunctional CuNi-*x* Nano-alloys for electrocatalytic nitrate reduction and HPAM oxidation coupling reactions. *Mater. Chem. Front.* **2025**, *9*, 638–647.

Liqing Li, received his B.S. degree from China University of Geosciences, Wuhan in 2023. Currently, he is pursuing a master's degree in the College of Materials Science and Engineering, Harbin University of Science and Technology. His research interests include the synthesis of metal-organic frameworks and their related performance in the electrocatalytic reduction of nitrate to ammonia.

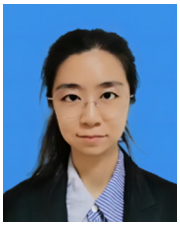

Xinming Wang, received her Bachelor's degree from Northeast Agricultural University in 2008, followed by a Master's degree in 2011. She received her Ph.D. from Harbin Institute of Technology in 2015. Currently an associate professor at the School of Materials Science and Chemical Engineering, Harbin University of Science and Technology, her research focuses on: design and synthesize inorganic-organic hybrid materials and polyoxometalate-based materials; the surface modification and self-assembly of electrodes for electrocatalytic ammonia synthesis and hydrogen production; the development of high-performance supercapacitors; and the implementation of photocatalytic water splitting technologies.

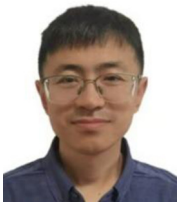

Haijun Pang, received his BS degree in chemistry from Harbin Normal University in 2005. He gained his Ph.D. under the supervision of Prof. Jun Peng and Prof. Yaguang Chen at Institute of Polyoxometalate Chemistry, Northeast Normal University in 2010. In the same year, he started his career as a lecturer at Harbin University of Science and Technology, and became a full professor of chemical engineering and technology at Harbin University of Science and Technology in 2018. His current research focuses on polyoxometalate-based materials for photocatalysis/electrocatalysis, supercapacitors, and electrochemical sensors